Application of the ENS3DAE Euler/Navier-Stokes Aeroelastic Method

David M. Schuster
NASA Langley Research Center
Hampton, Virginia 23681-0001 USA

Philip S. Beran
Air Force Institute of Technology
Wright Patterson AFB, Ohio 45433 USA

Lawrence J. Huttsell
Air Force Research Laboratory
Wright Patterson AFB, Ohio 45433 USA

SUMMARY

This paper discusses recent applications of the ENS3DAE computational aeroelasticity method. In particular, it describes aeroelastic and unsteady aerodynamics calculations performed on wings with trailing edge control surfaces. These simulations include the investigation of control reversal for a structurally flexible wing with a deflected control surface, and a static and dynamic analysis of a rigid wing with an oscillating control surface. The two sets of calculations were performed independently on different wings using different grid topologies. The control reversal simulation represents an inviscid Euler static aeroelastic analysis of a thin wing with a rectangular planform. The geometry of this wing makes it suitable for computations using more approximate, inviscid aerodynamics methods. Thus, the results of the present Euler computations are compared with numerical data generated by a validated computational aeroelasticity code which uses a simpler aerodynamic formulation. The second illustrated case involves the simulation of a significantly more complex flowfield and the static and dynamic analyses of this geometry were performed using the viscous Navier-Stokes equation option in ENS3DAE. Results of both the steady and unsteady calculations on this wing are compared with existing experimental data.

INTRODUCTION

The ENS3DAE aeroelastic method[1] has been in development and use since 1989 when it was delivered to the Air Force Wright Laboratory by the then Lockheed Aeronautical Systems Company. Since that time, a number of static and dynamic, rigid and aeroelastic test cases have been analyzed using the program and the code has been validated against existing computational and experimental data. Research using the code has focused on applying the method to problems whose geometric and/or aerodynamic complexity are suited to analysis using the Euler/Navier-Stokes equations[2, 3]. Flows involving shock waves interacting with boundary layers, generation of vortices and separated boundary layers are among those that can and should be addressed using this class of method. These types of flows can be generated by vehicles operating deep in the transonic speed regime or at high angles-of-attack, or simply by geometric anomalies in the surface of the vehicle. An example of this latter mechanism is a deflected control surface.

Nonlinear aeroelasticity with control surface deflection has been investigated by Batina, et al.[4] and Guruswamy and Tu[5], both using inviscid transonic small disturbance potential flow theory as their aerodynamic basis. Pitt and Fuglsang[6] also investigated aileron reversal using this type of method. These simulations were performed on wings with thin airfoil sections and control surface deflections of one-half degree or less, thus avoiding violation of the inviscid small disturbance assumptions inherent in the aerodynamic analysis. The first application described in this paper examines the static aeroelastic deformation of a thin wing with a small control surface deflection. Control effectiveness and reversal is predicted using the Euler equation option of ENS3DAE and results are compared with those of Andersen, et al.'s[7] CAP-TSD[8] transonic small disturbance equation analyses.

Larger control surface deflections and thicker wing sections require higher-order aerodynamic simulations since inviscid methods classically overpredict the effectiveness of the control surface for these cases. Under these conditions, strong shocks and separated flow can form on the control surface. In addition, the sharp edges of the control surface combined with its increased loading can form local vortices which can interact with the rest of the lifting surface flowfield. In general, prediction of these features requires a viscous simulation. Obayashi[9, 10] has investigated a semispan wing and a full-span wing/fuselage configuration with oscillating control surfaces using three-dimensional Navier-Stokes aerodynamics. Both of these simulations modeled a thin wing with a trailing edge control surface. The full-span computations involved large control surface deflections, and complex interactions between the wing and control surface vortices were observed. The second case presented in this paper uses ENS3DAE to perform a viscous calculation for a wing with a simpler planform and a thick

airfoil section. Both static and oscillating trailing edge control surface deflections are simulated, and the unsteady computations are performed at a much lower reduced frequency than the referenced computations. These computations are compared with experimental benchmark data. Of particular importance are detailed comparisons of the unsteady pressure distributions due to control surface oscillation with unsteady experimental pressure data.

ENS3DAE AEROELASTIC METHOD

ENS3DAE solves the full three-dimensional compressible Reynolds averaged Navier-Stokes equations using an implicit central finite difference approximate factorization algorithm. The method accepts either single or multiple block curvilinear grid topologies and can be run in a steady state or time-accurate mode. Turbulence characteristics are predicted using the Baldwin-Lomax algebraic turbulence model or the Johnson-King model. For the present calculations, the Baldwin-Lomax model is used with transition assumed to be at the leading edge of the wing. A multigrid option for steady flows has recently been added to the method and the code has been explicitly written to take advantage of vectorization. Directives for parallel operation on shared memory processors are also included in the programming.

A linear generalized mode shape structural model is closely-coupled with the aerodynamic method to analyze structurally flexible vehicles. Since dynamic aeroelastic and oscillating control surface simulations require grid models that deform in time, a Geometric Conservation Law (GCL) patterned after that recommended by Thomas and Lombard[11] has also been incorporated in the code.

In the interest of brevity, the details of the numerical algorithm will not be discussed in this paper, and the reader is referred to Reference 1 and Reference 2 for a detailed description of the method.

WING GEOMETRIES

The wing geometries chosen for these studies are shown in Figure 1. Both have a rectangular planform and constant airfoil section from root to tip with no twist. The wing used for the static aeroelastic calculations is patterned after the so-called heavy Goland wing.[12] In this paper, the wing is simply referred to as the rectangular wing. This wing has a semispan of 20 feet and a chord of 6 feet. It includes a 25% chord trailing edge control surface, designated by the shaded area in the figure, that extends from the wing midspan to the tip. The airfoil for this wing is a 4% thick symmetrical parabolic arc section.

The oscillating control surface case was performed on the NASA Langley Benchmark Active Controls Technology (BACT)[13] wing. The BACT model is also a rectangular wing with a NACA 0012[14] airfoil section. The wing has a semispan of 32 in., and a chord of 16 in. It is fitted with a trailing edge

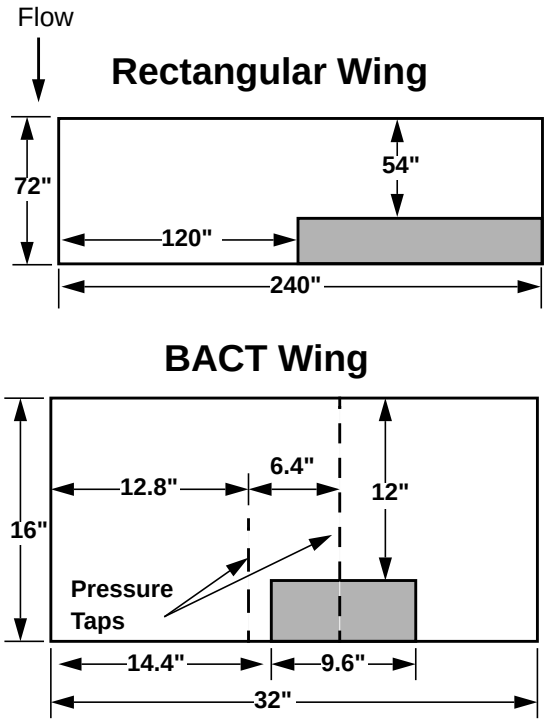

Figure 1. Planform views of rectangular and BACT wings.

control surface which extends from 45% span to 75% span and has a chord of 25% of the wing chord. The wind tunnel model also had upper and lower surface spoilers which are not depicted in the figure and were not simulated in this analysis. Experimental data for this wing included overall wing forces and moments as well as unsteady pressures. A row of pressure taps were located on the upper and lower surfaces of the wing at 60% span, which coincides with the spanwise center of the aileron. Pressures were measured from the wing leading edge to the trailing edge at this wing station. In addition, a second row of pressures were located at 40% span. At this location, upper and lower surface pressures were measured from 60% chord to the wing trailing edge.

Geometry Modeling and Grid Generation

Due to the differences in airfoil section, different grid topologies were used to model the two wings. Since the rectangular wing has a thin sharp-edged airfoil, a multizone H-H grid topology is employed for this lifting surface. A planform view of the grid for this configuration is shown in Figure 2. This figure is arranged vertically so that the wing root is at the bottom of the figure and the wing tip is at the top. The wing is modeled using two grid zones, one for the flowfield above the wing surface and the other below the wing.

Each zone consists of 120 points in the streamwise direction with 61 points distributed from the wing leading edge to the trailing edge. There are a total of 41 spanwise points with 33 of those stations extending from the wing root to the wing tip. Each zone uses 50 points normal to the wing surface to

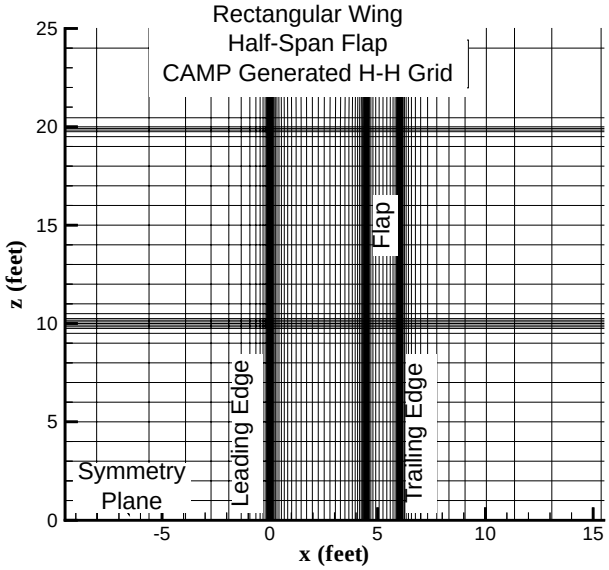

Figure 2. Planform view of rectangular wing grid.

complete the flowfield model. Thus a total of 492,000 grid points are used for this Euler simulation. The spanwise distribution of points was taken from the CAP-TSD grid used in Reference 7 so that a direct comparison could be made between ENS3DAE and CAP-TSD.

Figure 3 displays a section of the H-grid through the middle of the flap on the rectangular wing with the flap deflected one degree. Grid points are clustered at the wing section leading and trailing edge as well as near the control surface hinge line. The first grid line parallel to the airfoil surface is placed 0.0025 chords from the surface which is sufficiently close to the wing for the inviscid calculations to be performed on this geometry.

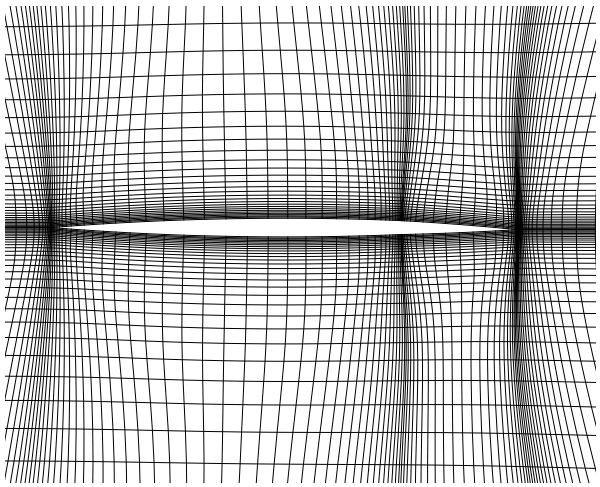

Figure 3. H-grid through rectangular wing section.

Since the BACT wing has a blunt leading edge, twelve percent thick airfoil section, a C-H grid topology is used to model this configuration. This grid consists of a total of 332,469 grid points distributed with 153 points in the wraparound or “C” direction, 53 points in the spanwise, or “H” direction, and 41 points from the wing surface to the outer boundary. An isometric view of the BACT surface grid with the aileron deflected -5^o is presented in Figure 4. The grid lines are placed in the spanwise direction so as to accurately define the edges of the trailing edge control surface. In addition, there is a grid line precisely at 40% and 60% span so that a direct comparison can be made with available experimental data. The streamwise distribution of grid points is also tailored to accurately model the aileron hinge line.

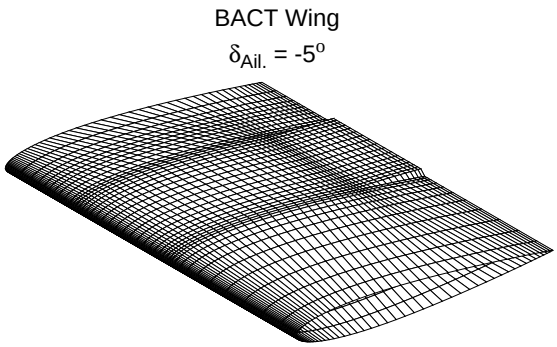

Figure 4. Isometric view of BACT wing surface grid, $\delta_{Ail.}$ = -5.0^o.

A side view of the viscous grid through the 60% span station is shown in Figure 5. The nominal wall spacing normal to the wing surface is 0.0002 chords at the leading edge, linearly increasing to 0.003 chords at the trailing edge. This spacing generates y^+ values less than 6 over the entire surface of the wing. This ensures that at least one grid point will be within the laminar sublayer of the boundary layer, which is required for accurate application of the turbulence model. The aileron deflection for the static cases is obtained by preprocessing the airfoil sections used to define the wing surface. A rigid body rotation of the trailing edge portion of the airfoil sections at the inboard and outboard edges of the control surface is performed to define new airfoil contours at these wing stations. The airfoils just inboard and just outboard of the aileron are left unchanged. The flowfield grid is then generated about this modified geometry using the same techniques as for the case where the aileron is not deflected. This effectively shears the baseline grid in the vicinity of the aileron to define the deflected control surface geometry. This method is simple and very efficient to implement. However, it results in a model which does not have gaps between the control surface and the main wing. This is not a significant problem in this analysis since these gaps are very small on the BACT model. This approximation also is more significant when large control surface deflections are to be simulated, but in this analysis our deflections have been limited to five degrees or less.

For cases where the aileron is oscillated, a mode shape describing the aileron deflection is input directly into the ENS3DAE program. The undeflected grid is used as the basis for the aerodynamic solution. The grid is deformed in time by

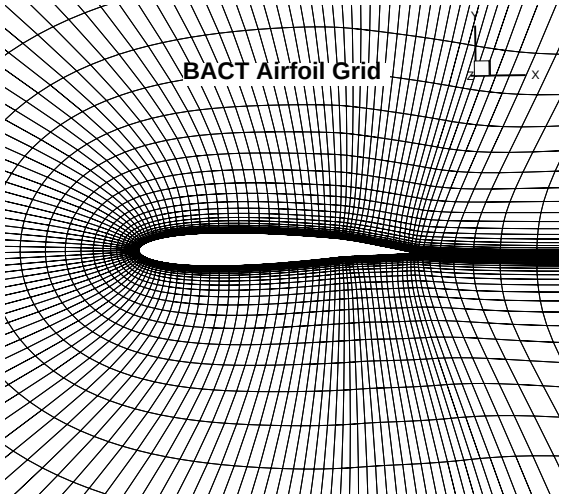

Figure 5. BACT airfoil section grid, $\delta_{Ail.} = 5.0^{o}$.

superimposing the aileron deflection mode shape on the baseline grid and using ENS3DAE's built-in grid motion capability to deflect the grid. Again, this method effectively shears the grid in the vicinity of the aileron and control surface gaps are not simulated. The mode shape is also defined as a deflection only in the vertical direction, so the chord of the control surface is stretched as the aileron is deflected. For small deflections, this stretching is negligible.

RESULTS

Static Aeroelastic Analysis of the Rectangular Wing

The rectangular wing was analyzed using the inviscid Euler equation option in ENS3DAE. The flow conditions for the analysis are Mach 0.7, zero degrees angle-of-attack and a static control surface deflection of one degree. The beam structural model of Reference 7 was used for all structurally flexible calculations performed on this wing.

An initial static rigid calculation was performed at the reference conditions to establish a basis for aileron control effectiveness. A series of structurally flexible simulations were then performed at steadily increasing dynamic pressure. The rolling moment at each dynamic pressure was computed and the ratio of the flexible rolling moment to the rigid rolling moment was calculated. A plot of this ratio as a function of dynamic pressure is presented in Figure 6. Included on this figure are CAP-TSD results from Reference 7. Control reversal occurs when the control effectiveness ratio becomes negative, as shown in the figure. ENS3DAE predicts a control reversal dynamic pressure of approximately 310 pounds per square foot (psf) compared to CAP-TSD's prediction of 335 psf or an eight percent difference. The ENS3DAE and CAP-TSD results were computed with the same spanwise grid distributions, and similar streamwise grid point distributions. However, ENS3DAE's vertical grid resolution in the vicinity of the wing surface was finer than that used in the original CAP-TSD analysis shown as the upside down triangles in the figure. The CAP-TSD computation was rerun for dynamic pressures of 250 and 300 psf using the Euler analysis normal grid distribution. These results are shown as the diamonds in the figure. For this grid, CAP-TSD predicts an estimated reversal dynamic pressure of 319 psf which compares to within three percent of the Euler results. These results illustrate that grid refinement plays a significant role in this analysis and further investigation into these effects are under way.

Figure 7 compares the ENS3DAE and CAP-TSD pressure distributions as a function of the streamwise coordinate along the midspan of the flap for the 300 psf dynamic pressure. The Euler analysis is depicted by the solid line, while the CAP-TSD analysis is shown by the symbols. These pressure distributions were chosen since they are near the point of reversal. The CAP-TSD and Euler calculations compare very closely for this case, as would be expected for this configuration at these flight conditions. In general, the Euler analysis predicts sharper, deeper pressure peaks in the vicinity of the wing leading and trailing edges, and at the control surface hinge line. These results provide confidence that the ENS3DAE method is predicting accurate results for relatively benign flight conditions, and we are ready to apply the method to more challenging problems. Transonic and low supersonic calculations are currently being computed using ENS3DAE, and these data will be similarly compared with CAP-TSD results.

BACT Wing Static Analyses

Static and dynamic rigid calculations were performed on the BACT wing with ENS3DAE providing viscous full Reynolds-averaged Navier-Stokes simulations. These calculations were compared with experimental data acquired in heavy gas in NASA Langley Research Center's Transonic Dynamics Tunnel (TDT). The nominal flight conditions for these calculations are Mach 0.77 and a Reynolds number of 280,000/ft., which coincide with the test data acquired in the TDT.

Prior to computing the flowfield for the wing with the deflected aileron, a number of calculations were performed on the basic wing without control surface deflection. Inviscid Euler and viscous Navier-Stokes calculations were performed on the wing for both nonlifting and lifting cases. Detailed description of the Euler computations have been omitted from this discussion, but there are several notable features of the Euler analysis which should be addressed. As expected, shock strength was greater for the inviscid calculations, and the shock was displaced aft of the viscous analysis. Viscous effects were also clearly visible in the surface pressure distribution near the trailing edge of the wing. In this region, the inviscid pressures recovered to a significantly higher stagnation pressure than their viscous counterparts. This difference is due to the thickening of the boundary layer near the trailing edge, which tends to flatten the curvature of the airfoil in this region. This effect is even more pronounced when the control surface is deflected, and is the primary reason why inviscid methods cannot generally be applied to this problem.

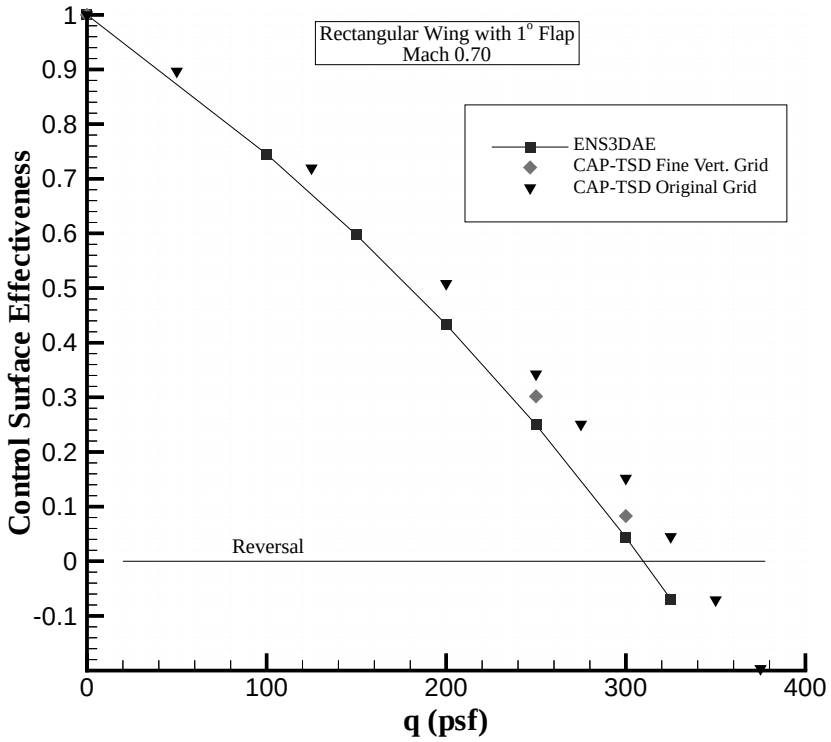

Figure 6. Aileron control effectiveness as a function of dynamic pressure for the rectangular wing, M=0.7, α=0.0°, $\delta_{Ail.}$=1.0°.

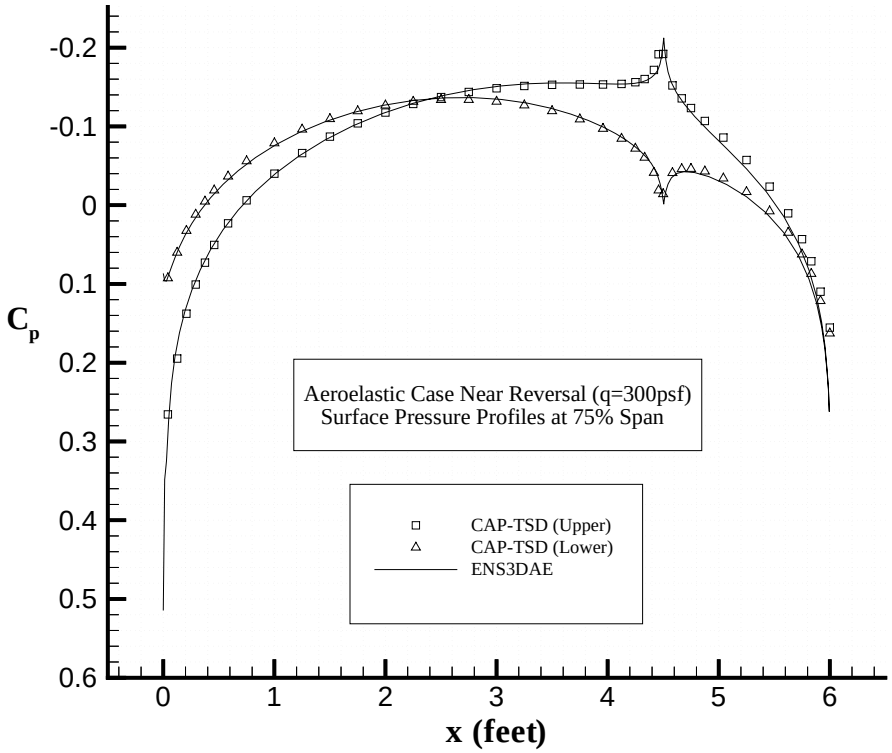

Figure 7. Rectangular wing pressure distribution near reversal, M=0.7, α=0.0°, $\delta_{Ail.}$=1.0°, q=300 psf.

Figure 8 presents the viscous computation of the flow at M=0.77, and zero degrees angle-of-attack. For this nonlifting case, the computations compare relatively well with the experimental data acquired in the TDT. The theory predicts a slightly lower pressure on the forward portion of the wing at the 60% span station, but the pressures on the remainder of the wing are in good agreement with the experimental data.

ENS3DAE calculations are compared with experimental data at M=0.77 and $\alpha=3^o$ in Figure 9. At these conditions, a shock on the upper surface is clearly visible in both the theoretical and experimental data. The lower surface pressure distribution and the pressures behind the shock are accurately predicted by the theory. However, the pressure distributions do not compare well on the forward portion of the wing upper surface. This area is usually insensitive to viscous effects since the boundary layer is thin and the flow is experiencing a favorable pressure gradient. However, a sharp increase in the experimental pressure is observed on the 60% span upper surface at 5% chord. This sudden increase is speculated to be due to the transition strip on the model, and the strip could be affecting the flow downstream. The theory accurately predicts the pressure forward of 5% chord. A second possibility for this poor correlation is aerodynamic interactions between the model and the wind tunnel which are not accounted for in the analysis. In addition to the wind tunnel walls, there are several model support components including a splitter plate, and an instrumentation housing which add to the blockage of the tunnel. All computations to date have been performed without modeling the wind tunnel walls or support structure.

Static calculations were also performed with aileron deflection. Figure 10 shows the pressure distribution for an ENS3DAE Navier-Stokes calculation at M=0.77, $\alpha=0.0^o$, and $\delta_{Ail.}=5.0^o$. At these conditions, lift is generated by the wing due to the flap deflection. Once again, the theoretical and experimental pressures agree well on the aft portion of the wing, and on the entire lower surface. However, as with the previous lifting cases, the upper surface pressure on the forward portion of the wing does not agree well with the experimental data. The theory predicts a consistently lower pressure on this part of the wing.

ENS3DAE was run for a total of 2000 iterations for these steady Navier-Stokes analyses, and the L-2 norm of the density residual is reduced by approximately 2.5 orders of magnitude during this period. By iteration 2000, oscillations in the lift and pitching moment coefficient have reduced to a very small amplitude and can be considered at a steady state for this analysis. Noticeable oscillations in the drag coefficient were still present at this point in the solution. To further investigate the convergence characteristics of this problem, a viscous solution at $\alpha=2^o$ was run a total of 4000 iterations and the drag was shown to reach a steady state at approximately 2500 iterations. The differences in the pressure distributions between 2000 and 4000 iterations were virtually indiscernible. Therefore, for the purposes of this study, all static simulations were assumed to be at a steady state after 2000 iterations.

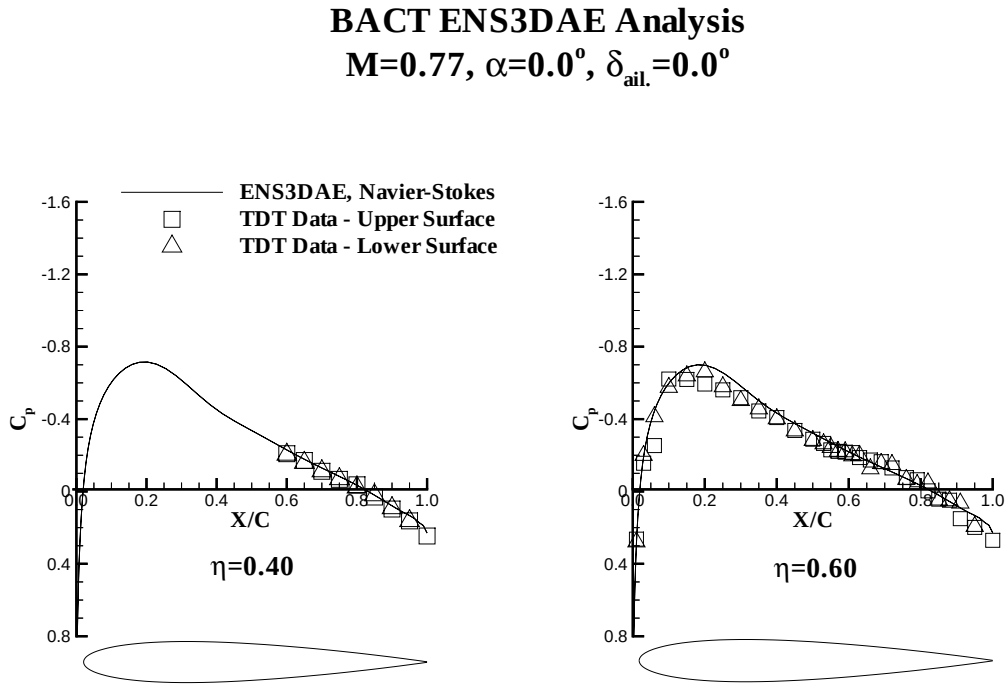

Figure 8. Steady viscous pressure distribution on BACT wing at M=0.77, $\alpha=0.0^o$, $\delta_{Ail.}=0.0^o$.

BACT ENS3DAE Analysis
M=0.77, α=3.0^o, $\delta_{ail.}$=0.0^o

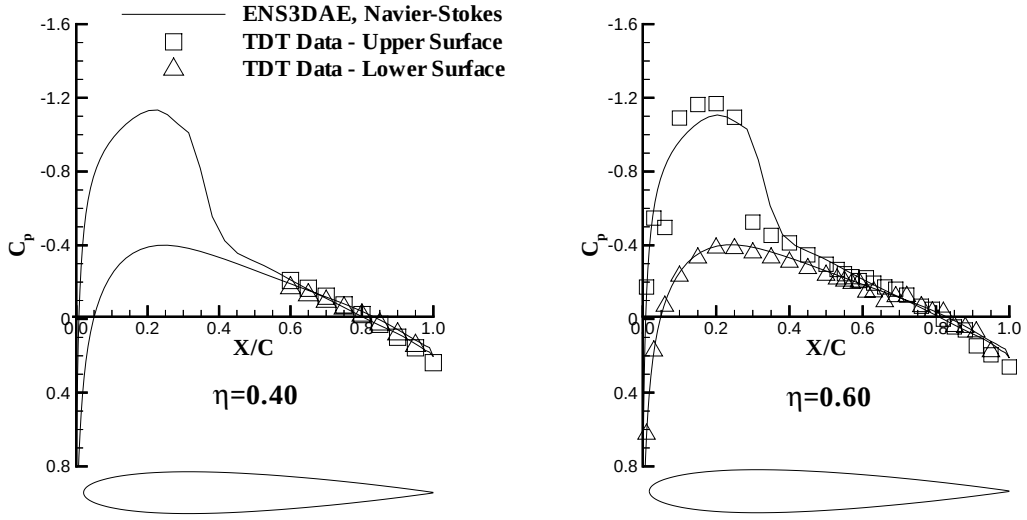

Figure 9. Steady viscous pressure distribution on BACT wing at M=0.77, α=3.0^o, $\delta_{Ail.}$=0.0^o.

BACT ENS3DAE Analysis
M=0.77, α=0.0^o, $\delta_{ail.}$=5.0^o

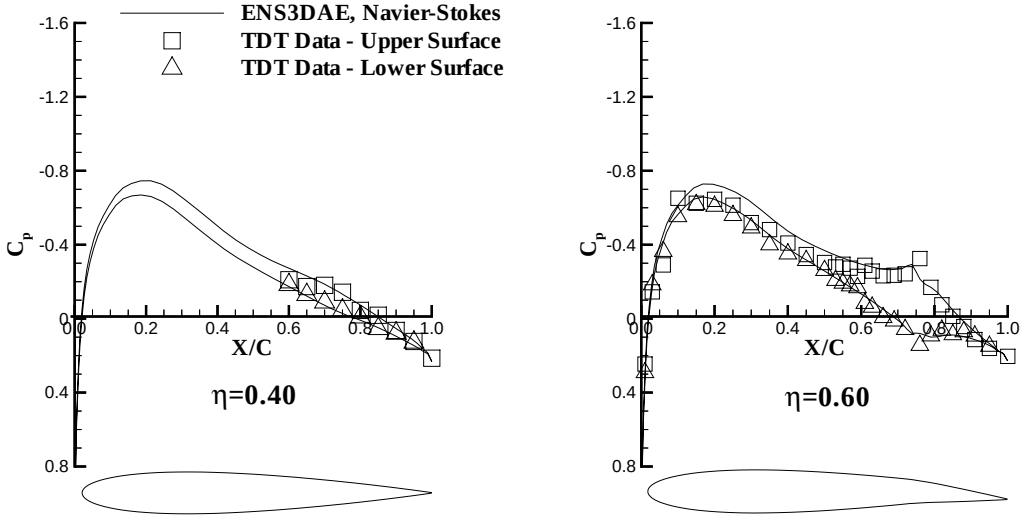

Figure 10. Steady viscous pressure distribution on BACT wing at M=0.77, α=0.0^o, $\delta_{Ail.}$=5.0^o.

Unsteady Analysis of BACT Wing with Oscillating Aileron

Unsteady simulations have been performed by harmonically oscillating the BACT aileron at a specified frequency. The unsteady computations are performed by using a steady solution about the baseline condition without aileron deflection, then impulsively starting the aileron oscillation. The solution is allowed to run until a total of three cycles of aileron oscillation are completed. For the simulations presented in this paper, the aileron is oscillated sinusoidally with an amplitude of two degrees at a frequency of five Hertz (Hz), which corresponds to a reduced frequency of 0.056 based on wing semichord.

An initial calculation was performed using a nondimensional time step of 0.1172 which for this problem is a CFL number of approximately 90 based on the global minimum time step for this grid. This CFL number is well beyond where we had previously run the code, and we felt that these conditions might be near the algorithm's stability limit. With this time step, one cycle of aileron oscillation at 5 Hz requires 10,000 time steps. Thus, it required 30,000 time steps to complete the three cycles of motion. Once this initial transient was successfully completed, we searched for the largest time step we could take and have the code remain stable. We were ultimately able to double the time step to 0.2344, which gave us a CFL number of 180 and reduced our run time to 5,000 time steps per cycle of aileron oscillation. Upon comparing these two analyses, no noticeable differences in the results were observed.

Figure 11 shows the unsteady pressure at 60% span and 23% chord for the 5,000 time step per cycle simulation. The pressure is plotted against nondimensional time, and the aileron deflection angle as a function of time is included at the bottom of the figure. Following an initial transient due to the impulsive start of the aileron oscillation, the pressure at this station quickly becomes sinusoidal and by the end of the first cycle of aileron oscillation, it has stabilized into a clean periodic form. The pressure distributions due to the second and third cycles of aileron motion are virtually identical giving us good confidence that the solution has reached a stable periodic response by the end of the second cycle of aileron deflection. Pressure distributions at other wing stations show similar character.

The unsteady pressures at the 40% and 60% span station were analyzed by taking the Fast Fourier Transform (FFT) of the pressures during the third cycle of aileron motion and scaling the real and imaginary components by the amplitude of the aileron deflection. In the following figures, the real component of the unsteady pressure represents the pressure perturbation that is in-phase with the aileron motion, while the imaginary component represents the pressure perturbation whose phase lags the aileron motion by ninety degrees. In addition, the mean pressure coefficient has also been extracted from the unsteady pressure.

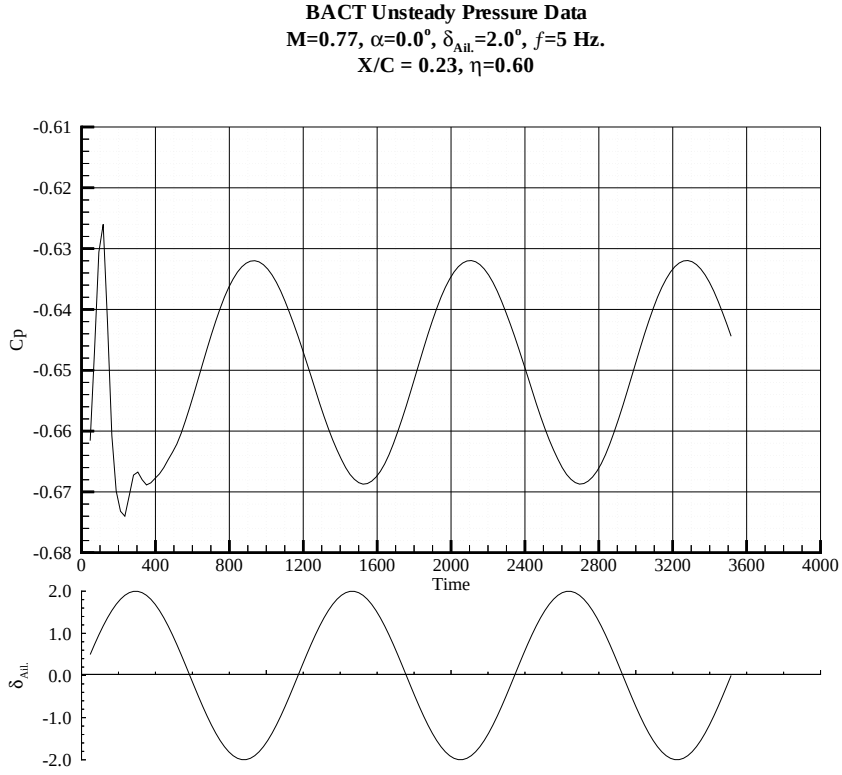

Figure 11. Unsteady BACT pressures M=0.77, α=0.0°, $\delta_{Ail.}$=2.0°, f=5 Hz.

Figure 12 compares the predicted mean pressure coefficient for the unsteady analysis with the TDT experimental data. The agreement for this case is similar to that obtained for the steady analysis. This figure is significant since this is a comparison of mean values extracted from the unsteady pressure data. This pressure distribution is an important contributor to the overall pressures computed by the analysis method, which is often overlooked when evaluating unsteady simulations. The favorable mean pressure comparison with experimental data is the first indicator that the computational method is providing an accurate temporal simulation. If there were errors in the temporal algorithm they would very likely be uncovered by this comparison.

Figure 13 compares the in-phase and out-of-phase perturbation pressures at the 40% span, while Figure 14 presents this same comparison at 60% span. Both of these figures show that the pressure coefficient response to the aileron deflection is primarily in-phase with the aileron motion since the real components of the pressures are noticeably larger in amplitude than the imaginary components. The comparison of both the real and imaginary components of pressure with the experimental data are very good at the 40% span station. The comparison is also good for the real pressure at 60% span from 60% chord aft. In Figure 14 a definite jump in the experimental real component of the pressure can be seen at 60% chord. The aileron extends from 75% chord aft, and the agreement between theory and experiment on this portion of the wing is excellent. The BACT also has a deployable spoiler at this station which extends from 60% chord to 75% chord. The pressure distribution comparison in this area is also very good. The wing ahead of 60% chord is fixed and does not house any control surfaces. It is in this area that the theory and experiment do not compare well. The sharp jump in the experimental data at 60% chord combined with the excellent agreement between theory and experiment on the spoiler and oscillating aileron suggest that there may be an anomaly in the experimental data where the model transitions from the fixed portion of the wing to the control surfaces. However, a preliminary investigation into the experimental data has not uncovered any obvious deficiencies. Investigations with other numerical methods may provide further insight into these differences, and these calculations are planned for the near future.

CONCLUSION

The ENS3DAE computational aeroelasticity program has been applied to the static aeroelastic and the unsteady aerodynamic analysis of two rectangular wings. Both wings included trailing edge control surfaces, which were deflected during the analysis. The static aeroelastic calculations investigated control reversal on a thin wing with a parabolic arc airfoil. Results of this study have been compared with results obtained using the CAP-TSD computational aeroelasticity program, which is based on transonic small disturbance potential flow aerodynamics. Detailed comparisons of the pressure distributions at the mid-span of the control surface show

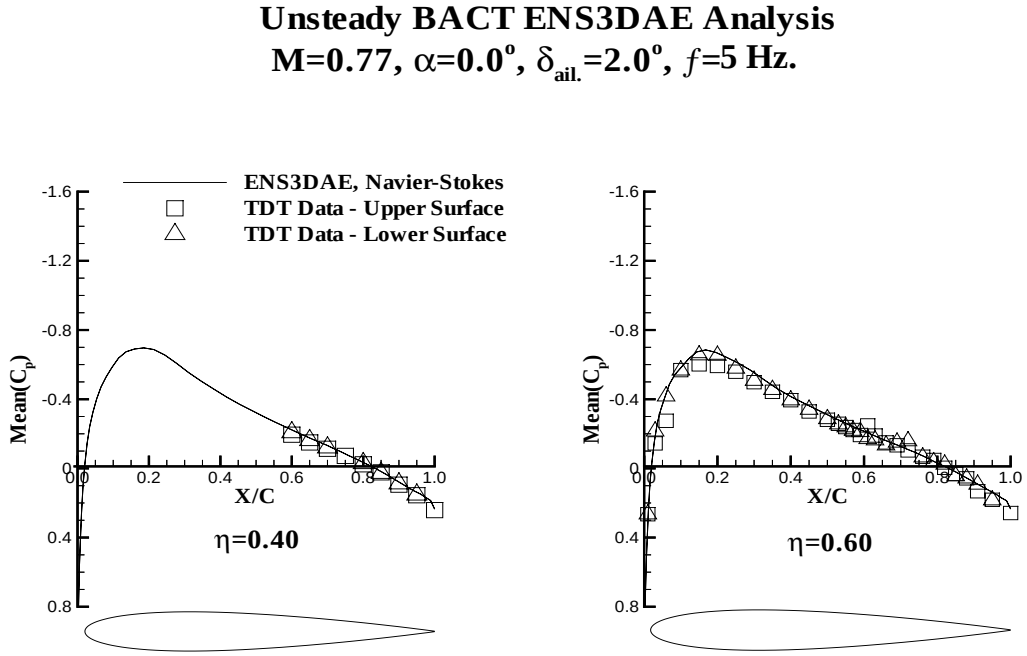

Figure 12. Mean unsteady BACT pressures, M=0.77, α=0.0°, $\delta_{Ail.}$=2.0°, f=5 Hz.

Unsteady BACT ENS3DAE Analysis
M=0.77, α=0.0°, $\delta_{Ail.}$=2.0°, f=5 Hz.
η = 0.40

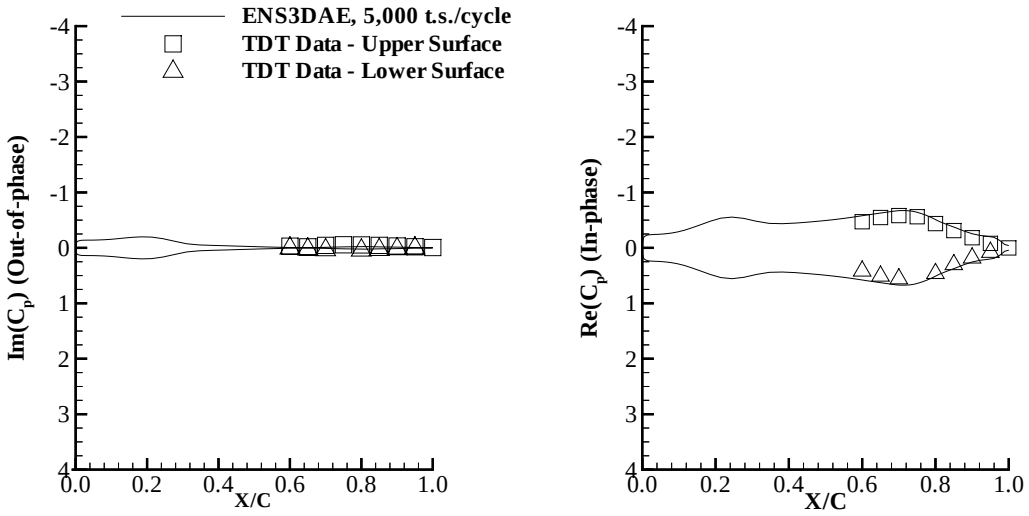

Figure 13. Unsteady BACT pressures M=0.77, α=0.0°, $\delta_{Ail.}$=2.0°, f=5 Hz, η=0.40.

Unsteady BACT ENS3DAE Analysis
M=0.77, α=0.0°, $\delta_{Ail.}$=2.0°, f=5 Hz.
η = 0.60

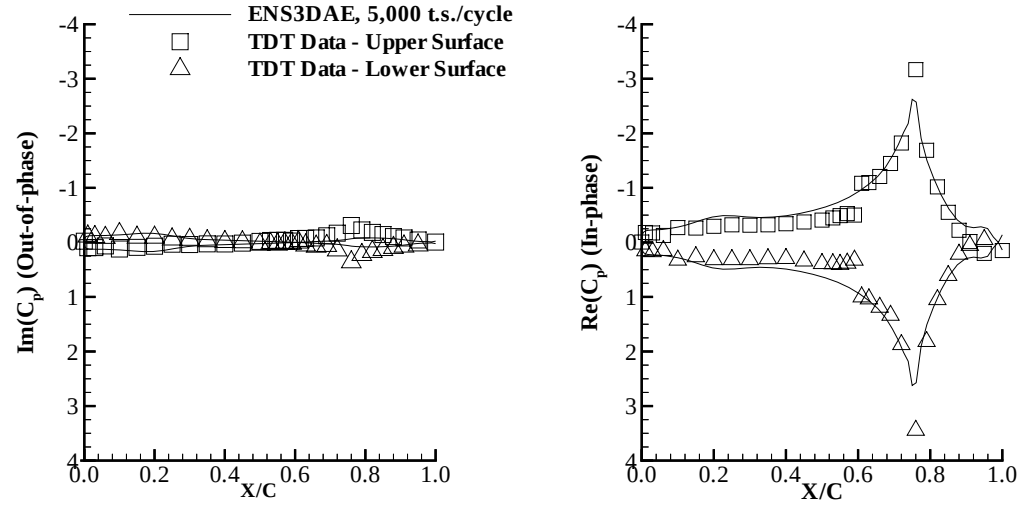

Figure 14.Unsteady BACT pressures M=0.77, α=0.0°, $\delta_{Ail.}$=2.0°, f=5 Hz, η=0.60.

expected excellent agreement between the ENS3DAE Euler equation analysis and CAP-TSD. The control reversal dynamic pressure predicted by ENS3DAE is approximately three percent lower than that computed by CAP-TSD. This parameter has been shown to be sensitive to the distribution of grid points in the CAP-TSD analysis and further grid resolution studies on both methods are currently underway.

Steady and unsteady Navier-Stokes equation calculations were performed on the BACT wing with a fixed and oscillating trailing edge control surface. Computed results have been compared with experimental data obtained in NASA Langley's Transonic Dynamics Tunnel. Cases where the flow is primarily subsonic over the entire surface of the wing section compare very well with experimental data. However, cases involving transonic flow show a discrepancy in the pressures on the forward portion of the airfoil upper surface and in the shock strength and location. Transonic pressures ahead of shock waves are typically well-predicted by computational methods, leading us to believe that there may be complex interactions between the wind tunnel and the model that are not accurately accounted for in our numerical analysis. Mean pressures from the unsteady aileron deflection analysis compare very well with the experimental data. The in-phase component is the main contributor to the unsteady pressure perturbation, and these computations compare closely with the TDT data from 60% chord aft. Differences on the forward portion of the wing similar to those observed in the steady analysis are also present in the unsteady perturbation pressures. The out-of-phase pressure component is considerably smaller in magnitude than the in-phase component, and given these small values, the comparison between theory and experiment is reasonable. Further calculations modeling the wind tunnel walls and support structure are required to investigate the transonic differences between the theoretical and experimental data.

ACKNOWLEDGEMENTS

Portions of this work were supported by the Air Force Research Laboratory under Contract F33615-95-D-3214, DO 0003, "Validation of ENS3DAE (Time Accurate Calculations)." The authors would like to thank Dr. Raymond Kolonay of the Air Force Research Laboratory for providing the additional CAP-TSD data presented in this report. The computational resources for these investigations were provided by the U.S. Army Corps of Engineers Waterways Experiment Station (CEWES), the Wright-Patterson Air Force Base Aeronautical Systems Center (ASC), and the Naval Oceanographic Office (NAVOCEANO) Major Shared Resource Centers.

REFERENCES

1. Schuster, D. M., J. Vadyak, and E. Atta, "Flight Loads Prediction Methods for Fighter Aircraft," WRDC-TR-89-3104, November, 1989.
2. Schuster, D. M., J. Vadyak, and E. Atta, "Static Aeroelastic Analysis of Fighter Aircraft Using a Three-Dimensional Navier-Stokes Algorithm," *Journal of Aircraft*, Volume 27, Number 9, September, 1990, pp. 820-825.
3. Schuster, D. M., "Application of Navier-Stokes Aeroelastic Methods to Improve Fighter Wing Performance," *Journal of Aircraft*, Volume 32, Number 1, January-February, 1995, pp. 77-83.
4. Batina, J. T., et al., "Unsteady Transonic Flow Calculations for Realistic Aircraft Configurations," *Journal of Aircraft*, Volume 26, Number 1, January, 1989, pp. 21-28.
5. Guruswamy, G. P. and E. L. Tu, "Transonic Aeroelasticity of Fighter Wings with Active Control Surfaces," *Journal of Aircraft*, Volume 26, Number 7, July, 1989, pp. 682-684.
6. Pitt, D. M., and D. F. Fuglsang, "Aeroelastic Calculations for Fighter Aircraft Using the Transonic Small Disturbance Equation," AGARD-CP-507, March, 1992, pp. 16-1 - 16-11.
7. Andersen, G., R. Kolonay, and F. Eastep, "Control Reversal in the Transonic Regime," AIAA Paper 97-1385, 38th AIAA/ASME/ASCE/AHS/ASC Structures, Structural Dynamics, and Materials Conference and Exhibit, Kissimmee, FL, April, 1997.
8. Batina, J. T., "A Finite-Difference Approximate-Factorization Algorithm for Solution of the Unsteady Transonic Small Disturbance Equation," NASA Technical Paper 3129, January, 1992.
9. Obayashi, S. and G. P. Guruswamy, "Navier-Stokes Computations for Oscillating Control Surfaces," *Journal of Aircraft*, Volume 31, Number 3, May-June, 1994, pp. 631-636.
10. Obayashi, S., I.-T. Chiu, and G. P. Guruswamy, "Navier-Stokes Computations on Full Wing-Body Configuration with Oscillating Control Surfaces," *Journal of Aircraft*, Volume 32, Number 6, November-December, 1995, pp.1227-1233.
11. Thomas, P. D., and C. K. Lombard, "Geometric Conservation Law and Its Application to Flow Computations on Moving Grids," *AIAA Journal*, Volume 17, Number 10, October, 1979, pp. 1030 - 1037.
12. Borland, C. J., "XTRAN3S - Transonic Steady and Unsteady Aerodynamics for Aeroelastic Applications," AFWAL-TR-85-3214, Air Force Wright Aeronautical Laboratories, Wright-Patterson AFB, OH, January, 1986.
13. Scott, R. C., et al., "The Benchmark Active Controls Technology Model Aerodynamic Data," AIAA Paper 97-0829, 35th Aerospace Sciences Meeting and Exhibit, January, 1997.
14. Abbott, I. H. and A. E. Von Doenhoff, *Theory of Wing Sections*, Dover Publications, Inc., New York, NY, 1959.